Performance of the Dragonfly Lander's Coaxial Rotor in Vortex Ring State

Michael A. Marshall* and Ellande Tang†
The Johns Hopkins University Applied Physics Laboratory, Laurel, Maryland, 20723

Jason K. Cornelius‡
NASA Ames Research Center, Moffett Field, California, 94035

J. Felipe Ruiz§
The Johns Hopkins University Applied Physics Laboratory, Laurel, Maryland, 20723

Sven Schmitz¶
The Pennsylvania State University, University Park, Pennsylvania, 16802

Dragonfly is a NASA New Frontiers mission with the goal of flying an autonomous relocatable rotorcraft lander to explore the surface of Saturn's moon Titan in the mid-2030s. The Dragonfly lander is an RPM-controlled multirotor with four coaxial rotor pairs, each with two counter-rotating two-bladed fixed-pitch rotors. To support the lander's development, the Dragonfly Team conducted a wind tunnel test campaign in September 2022 in the Transonic Dynamics Tunnel (TDT) at NASA's Langley Research Center. Due to Dragonfly's concept of operations, especially its transition to powered flight after atmospheric entry, Dragonfly must transition through and operate near a potentially hazardous flight regime called Vortex Ring State (VRS). For this reason, achieving safe flight on Titan requires an investigation of Dragonfly's VRS regime. To that end, this paper uses TDT measurements in a Titan-surrogate environment (R-134a) and computational fluid dynamics to study the performance of a flight-like coaxial rotor system in VRS. The analysis suggests that Dragonfly's coaxial rotor system is potentially more robust to the onset of VRS than an isolated single rotor with the same design, i.e., VRS initiates at a higher descent rate, and that some of the characteristics of the subsequent VRS are different. Consequently, these results have important implications for the design and operation of Dragonfly, along with other eVTOL aircraft destined for both terrestrial and extraterrestrial applications.

Nomenclature

A	=	rotor disk area, πR^2
C_{P_0}	=	profile power coefficient, $P_0/(\rho A(\Omega R)^3)$
C_T	=	rotor thrust coefficient, $T/(\rho A(\Omega R)^2)$
C_Q	=	rotor torque coefficient, $Q/(\rho A(\Omega R)^2 R)$
P	=	mechanical (shaft) power, W
P_c	=	climb power, W
P_i	=	induced power, W
P_0	=	profile power, W
Q	=	rotor mechanical torque, Nm
R	=	rotor blade radius, m
T	=	rotor thrust, N

*Guidance and Control Analyst, Space Exploration Sector, 11100 Johns Hopkins Road. Member AIAA. michael.a.marshall@jhuapl.edu

†Guidance and Control Analyst, Space Exploration Sector, 11100 Johns Hopkins Road. Member AIAA. ellande.tang@jhuapl.edu

‡Research Engineer, NASA Ames Research Center. Member AIAA. jason.k.cornelius@nasa.gov

§Mechanical Engineer, Space Exploration Sector, 11100 Johns Hopkins Road. felipe.ruiz@jhuapl.edu

¶Boeing/A. D. Welliver Professor, Department of Aerospace Engineering, 232B Hammond Building. AIAA Associate Fellow. sus52@psu.edu

v_h	=	hover induced velocity, $\sqrt{T/(2\rho A)}$
v_i	=	induced velocity, m/s
v_x, v_z	=	components of V_∞ parallel and perpendicular to rotor disk ($v_z > 0$ for climb), m/s
V_∞	=	wind tunnel freestream speed, m/s
α	=	rotor shaft angle relative to freestream (positive in descent), rad or deg
κ	=	induced power factor (typically 1.15)
μ_z	=	rotor axial advance ratio, i.e., rotor advance ratio perpendicular to rotor disk, $v_z/(\Omega R)$
ρ	=	fluid density, kg/m³
Ω	=	rotor speed, rad/s or RPM

I. Introduction

DRAGONFLY is a NASA New Frontiers mission that aims to assess the surface composition and prebiotic chemistry of Saturn's moon Titan in the mid-2030s using an autonomous relocatable rotorcraft lander [1, 2]. Titan's low gravity (approximately 1/7 Earth's) and dense atmosphere (approximately four times Earth's) reduce the power required for heavier-than-air flight by an order of magnitude or more relative to Earth [3, 4]. The electrically powered Dragonfly lander (hereafter often simply referred to as Dragonfly, see Fig. 1) takes advantage of these favorable environmental conditions to make short-distance (on the order of several kilometers), short-duration (on the order of ten minutes) relocation flights. During its approximately 3.3-year nominal mission, a series of flights can enable Dragonfly to potentially traverse over one hundred kilometers and make scientific observations at multiple geologically diverse locations on Titan's surface.
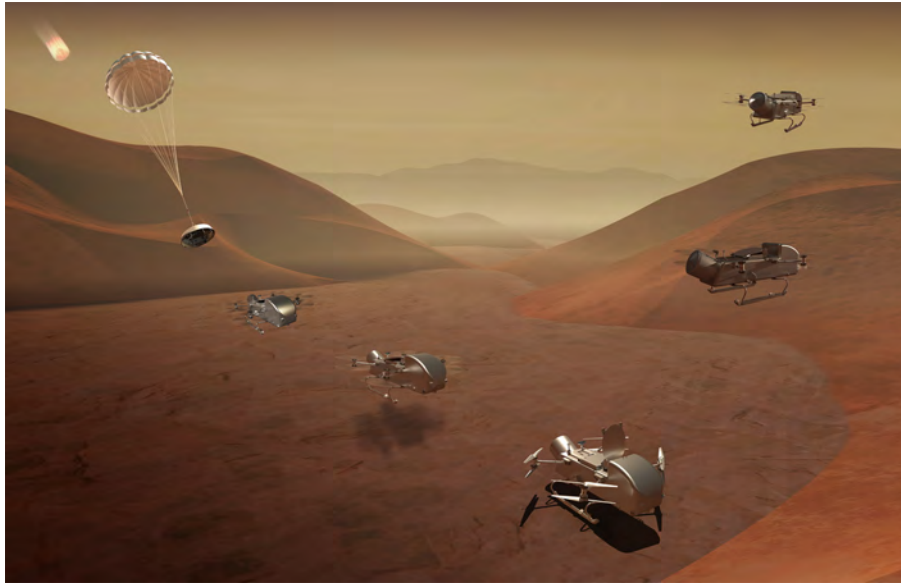

Fig. 1 An artist's impression of Dragonfly on the surface of Titan. Image courtesy of NASA/Johns Hopkins APL/Steve Gribben (`https://dragonfly.jhuapl.edu/Gallery/`).

To leverage terrestrial flight heritage, Dragonfly's design is inspired by the designs of conventional terrestrial multirotors (which for the purposes of this paper is a category of rotorcraft that encompasses small-scale drones, eVTOLs, and tiltrotors such as the Bell Boeing V-22 Osprey). Dragonfly is specifically an RPM-controlled multirotor with four counter-rotating coaxial rotor pairs arranged on its fuselage in an X8 configuration [1]; see Fig. 1. Compared to single rotors, counter-rotating coaxial rotors are advantageous because they balance the total torque on the lander and increase the thrust per unit of rotor disk area [5]. The latter is particularly important for maximizing the thrust for a multirotor that stows within the aeroshell required for Titan atmospheric entry [4].

Multirotors are particularly susceptible to the effects of a potentially hazardous flight regime called Vortex Ring State (VRS) [6–9]. VRS occurs when a rotor's descent rate approaches its wake speed. When this happens, the rotor blade tip vortices are no longer continuously convected away from the rotor disk; instead, the blade tip vortices form a toroidal vortex ring in the vicinity of the rotor. The vortex ring strengthens until it ultimately separates and convects away from the rotor disk plane. This repeating cycle of vortex ring buildup and separation is responsible for large fluctuations in the aerodynamic loads on the rotor [10]. The resulting high-amplitude, low-frequency unsteady aero-

dynamic loads can challenge flight dynamics, destabilize flight control systems, and in some cases, even lead to loss of control. In practice, VRS is avoided by either limiting the vertical descent rate or increasing the forward speed; for autonomous multirotors, this commonly manifests as a constraint on the flight trajectory (see e.g., [11–13]). The locus of constraints that denote the transition into VRS is commonly referred to as the VRS boundary [6, 14–16].


Fig. 2   An artist's impression of Dragonfly's concept of operations consisting of entry, descent, and first landing; surface operations; and atmospheric flight on Titan. Image courtesy of NASA/Johns Hopkins APL/Steve Gribben/Magda Saina (`https://dragonfly.jhuapl.edu/Gallery/`).

Unlike most terrestrial rotorcraft, Dragonfly's concept of operations (Fig. 2) requires it to fly through VRS for up to several seconds during its transition to powered flight (TPF) maneuver [17, 18]. After Dragonfly's initial atmospheric entry, it will descend vertically to Titan's surface under parachute. At approximately 4 km above Titan's surface, Dragonfly will jettison its aeroshell (heat shield). Then at approximately 1 km above Titan's surface, Dragonfly will execute the TPF maneuver depicted in Fig. 3 to fly away from its backshell and parachute, after which it will steadily descend to Titan's surface under its own power. As discussed in [17], the TPF maneuver starts in Windmill Brake State (WBS) and requires transiting through both Turbulent Wake State (TWS) and VRS into the Normal Working State (NWS). The steady descent to Titan's surface then occurs in the NWS. Because Dragonfly is power constrained, maximizing its performance also requires operating close to the boundary between VRS and NWS during descending forward flight. Maximizing the lander's achievable descent rate decreases the power required for descent, which in turn increases the stored energy available for other phases of flight. For these reasons, achieving safe flight on Titan requires a detailed understanding of the performance of Dragonfly's coaxial rotor system in and around VRS. To that end, the purpose of this paper is to use experimental data from a recent wind tunnel test campaign and computational fluid dynamics (CFD) to quantify the onset and effects of VRS for Dragonfly's coaxial rotor system. This paper significantly expands on previous experimental and numerical studies from the Dragonfly Team; see e.g., [17, 19, 20].

As part of Dragonfly's risk reduction and model validation efforts, the Dragonfly Team conducted a wind tunnel test campaign in September 2022 in the Transonic Dynamics Tunnel (TDT) at NASA's Langley Research Center. The TDT is a closed-circuit, continuous-flow, variable-pressure wind tunnel with the capability to test in both air and R-134a. An important objective of the test campaign was to collect flight-relevant data pertaining to the performance of Dragonfly's Phase B* rotor installed in a full-scale, flight-like coaxial rotor system in VRS. This involved collecting aerodynamic load measurements throughout the VRS regime in R-134a. This VRS-relevant data and its comparisons with CFD are the subjects of this paper. Compared to air, R-134a has a higher density (3.98 kg/m³ versus 1.225 kg/m³) that more closely matches the expected Titan atmospheric density of 5.35 kg/m³. As a result, R-134a also more closely matches the expected Reynolds number and rotor blade tip Mach number on Titan.

This paper is organized as follows: Sec. II reviews the fundamentals of momentum theory for a rotor in axial (vertical) flight (Sec. II.A) and describes a procedure for the analysis of experimental VRS data (Sec. II.B). Sec. III
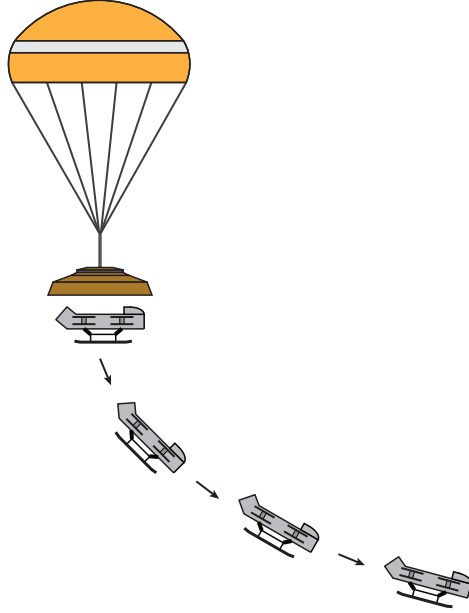
Fig. 3 Dragonfly's transition to powered flight (TPF) maneuver. During TPF, the lander separates from its backshell and pitches down to fly out of WBS, through TWS and VRS, and into NWS. TPF ends when the lander starts its steady-state descent to Titan's surface in NWS. Figure adapted from [17].

describes the design of Dragonfly's Phase B* rotor and the experimental setup in the TDT. Sec. IV provides a brief description of the CFD tool used to model the TDT test setup. Sec. V compares the TDT data with CFD and reports results for the unsteady aerodynamic fluctuations on the coaxial rotor system in VRS. Lastly, Sec. VI summarizes the paper's conclusions and their implications.

II. Background

This section first provides background on an empirical extension of momentum theory for modeling VRS (Sec. II.A). It then describes an analysis procedure for using rotor load measurements to quantify the magnitude of the thrust fluctuations in VRS (Sec. II.B).
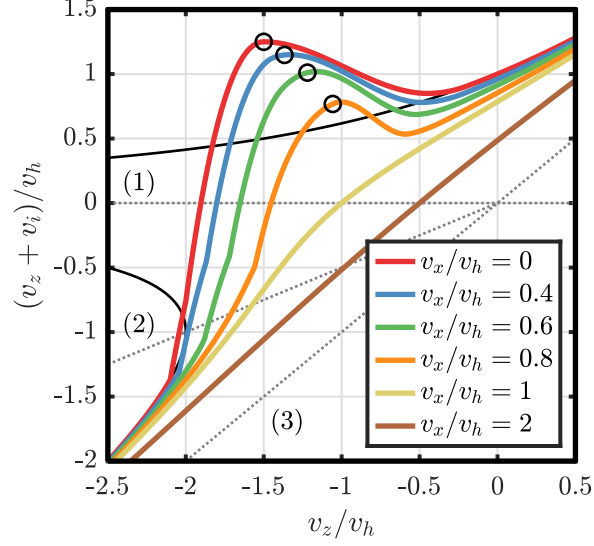
A. Review of Momentum Theory in Axial Flight

Momentum theory [10] models a rotor as an infinitely thin circular disk (an actuator disk) across which there is a discrete pressure jump. In the present context, the main utility of momentum theory is to provide a tool for calculating the rotor induced velocity v_i.

Using momentum theory, the axial flow through a rotor can be classified into four operating regimes based on the climb/descent speed v_z and v_i. These operating regimes, often referred to as inflow states, are Normal Working State (NWS, $v_z \geq 0$); Vortex Ring State (VRS, $v_z < 0$, $v_z + v_i > 0$); Turbulent Wake State (TWS, $v_z < 0$, $v_z + v_i < 0$, $v_z + 2v_i > 0$); and Windmill Brake State (WBS, $v_z < 0$, $v_z + 2v_i < 0$) [10]. Implicit to the derivation of momentum theory is the assumption that the velocity has a uniform direction throughout the flow field, i.e., there is no reverse flow. These assumptions are violated in VRS and TWS*. As a result, momentum theory is only valid in NWS and WBS.

Because momentum theory is not valid in VRS and TWS, a number of empirical relationships have been developed from experimental and/or flight test data to predict the induced velocity in and onset of VRS; see e.g., [6, 14–16]. In this paper, the VRS model originally introduced by Johnson [15] is used to predict the induced velocity in VRS (see Fig. 4). This VRS model (hereafter often referred to as the Johnson model) is a parametric polynomial extension of momentum theory in VRS and TWS used to calculate the mean rotor inflow. In Sec. V, the Johnson model is compared

---

*In practice, the momentum theory solution for climb in the NWS is a good approximation for small descent rates, but it begins to break down when $v_z \approx -v_h/2$ [10]. It follows that a more realistic boundary between VRS and TWS is the line $v_z + v_h/2 = 0$.

Fig. 4 VRS model from [15] used to predict the induced velocity v_i in VRS and TWS. The ∘ symbols denote points on the corresponding VRS boundary (defined for $v_x/v_h \leq 0.95$). The solid black lines denote the momentum theory solution in axial flight ($v_x/v_h = 0$). The dashed black lines are (1) $v_z + v_i = 0$, (2) $v_z + 2v_i = 0$, and (3) $v_i = 0$; the first and second denote the boundaries between VRS, TWS, and WBS.

with induced velocities derived from measurements in the TDT. Good agreement between Fig. 4 and the experimental results would suggest that the Johnson model is a reasonable predictor of VRS for Dragonfly's coaxial rotor system.
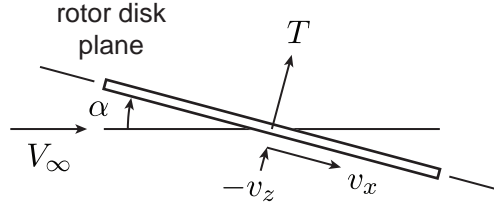
Fig. 5 Decomposition of freestream velocity V_∞ into components parallel to (v_x) and perpendicular to (v_z) to the rotor disk plane.

The VRS model in Fig. 4 is a function of the normalized components of the freestream velocity parallel to (v_x) and perpendicular to (v_z) the rotor disk plane (see Fig. 5):

$$v_x = V_\infty \cos(\alpha) \tag{1}$$

$$-v_z = V_\infty \sin(\alpha) \tag{2}$$

Here, V_∞ is the magnitude of the freestream velocity and α is the angle of attack of the rotor disk plane. For fixed-pitch rotors, α is often referred to as either the shaft angle or incidence angle; the former is preferred in what follows. The shaft angle is defined as positive for rearward tilt, i.e., $\alpha < 0$ for climb and $\alpha > 0$ for descent; $\alpha = 90$ deg corresponds to axial descent. Hover occurs when $V_\infty = 0$.

In Fig. 4, the components of the freestream velocity are normalized by the induced velocity at hover v_h. The momentum theory result for v_h is [10]

$$v_h = \sqrt{T/(2\rho A)} \tag{3}$$

where T is the thrust, ρ is the gas density, $A = \pi R^2$ is the rotor disk area, and R is the rotor blade radius. In this paper, Eq. (3) is evaluated for a coaxial rotor using the total combined thrust from the upper and lower rotors and the disk area of a single rotor in the coaxial pair (the projected disk area) [10].

Comparisons between the Johnson model and experimental data require an estimate of the mean induced velocity across the rotor disk. Following [15], the mean induced velocity across the rotor disk is defined as

$$v_i = P_i/(\kappa T) \tag{4}$$

where P_i is the induced power and κ is the induced power factor added for a non-ideal rotor. This paper uses the generic value of $\kappa = 1.15$ from [10]. Equation (4) implies that v_i can be estimated from the measured thrust and shaft power.

The total rotor mechanical (shaft) power P can be expressed as the sum of the induced power P_i, the climb power P_c, and the profile power P_0, i.e.,

$$P = P_i + P_c + P_0 \tag{5}$$

where $P = |Q|\Omega$, $P_i = \kappa T v_i$, $P_c = T v_z$, $P_0 = \rho A(\Omega R)^3 C_{P0}$, C_{P0} is the profile power coefficient, and $\Omega > 0$. The absolute value on Q reflects that the sign of Q depends on the rotor spin direction, but $P > 0$ irrespective of the spin direction. The mean induced velocity across the rotor disk can then be expressed as

$$v_i = \frac{|Q|\Omega - T v_z - \rho A(\Omega R)^3 C_{P0}}{\kappa T} \tag{6}$$

where T and Q are taken to be the mean measured thrust and torque. Alternatively, T and Q can be written in terms of the non-dimensional thrust coefficient C_T and torque coefficient C_Q, as follows [10]:

$$T = \rho A(\Omega R)^2 C_T \tag{7}$$

$$Q = \rho A(\Omega R)^2 R C_Q \tag{8}$$

Because $P = |Q|\Omega$, C_Q is equal to the rotor's mechanical power coefficient (up to a sign). An estimate for C_{P0} can then be derived analytically (e.g., from blade element theory), computed from CFD, or evaluated empirically from test data; the latter two approaches are used here. This paper assumes that C_{P0} is constant across the range of considered flight conditions. For this reason, C_{P0} is taken to be the profile power coefficient in hover. In hover, $v_i = v_h = \sqrt{T/(2\rho A)}$ and $v_z = 0$. Evaluating Eq. (6) in hover, substituting Eqs. (7) and (8), and rearranging yields the following expression for C_{P0}:

$$C_{P0} = |C_{Q0}| - \kappa\sqrt{C_{T0}^3/2} \tag{9}$$

Here, C_{T0} and C_{Q0} are the hover thrust and torque coefficients. Because Eqs (7) and (8) are quadratic in the thrust and torque coefficients, C_{T0} and C_{Q0} are estimated from the TDT data by fitting quadratic equations to the measured thrust and torque in hover. Equation (9) is then used to estimate C_{P0}.

Equations (7) and (8) give the typical definitions of the thrust coefficient C_T and the torque coefficient C_Q for an isolated rotor. These equations also apply to the upper and lower rotors in a coaxial pair. For a coaxial rotor, however, these definitions are modified as follows:

$$C_T^c = \left(C_T^u + C_T^\ell\right)\big/2 \tag{10}$$

$$C_Q^c = \left(-C_Q^u + C_Q^\ell\right)\big/2 \tag{11}$$

where the superscripts u, ℓ, and c denote the upper, lower, and coaxial rotors. Analogous definitions are used elsewhere; see e.g., [21]. With these definitions, C_T^c and C_Q^c are the mean thrust and torque coefficients per rotor in the coaxial pair. The torques on the counter-rotating upper and lower rotors have opposite signs. As a result, the negative sign on C_Q^u is necessary to preserve the equivalence between the mean coaxial torque and mechanical power coefficients. To simplify notation, the superscripts u, ℓ, and c are subsequently dropped.

Lastly, the Johnson model (Fig. 4) defines the onset of VRS as the locus of points where the inflow curve has zero slope, i.e., where $\mathrm{d}(v_z+v_i)/\mathrm{d}v_z = 0$ [15]. These points are denoted by the $\circ$ symbols in Fig. 4. The zero-slope condition on the inflow results in the following expression for the VRS boundary:

$$\left(\frac{v_z}{v_h}\right)_{\mathrm{VRS}} = \frac{v_{zN} + v_{zX}}{2} + \frac{v_{zN} - v_{zX}}{2}\left(1 - \left(\frac{v_x/v_h}{v_{xM}}\right)^2\right)^{0.2} \tag{12}$$

where $v_{xM} = 0.95$, $v_{zN} = -0.45$, and $v_{zX} = -1.50$. The following empirical relationship that matches momentum theory in axial flight is then used to predict the onset of WBS:

$$(v_z/v_h)_{\mathrm{WBS}} = -1.7/\sqrt{1 + (v_x/v_h)^2} \tag{13}$$

6
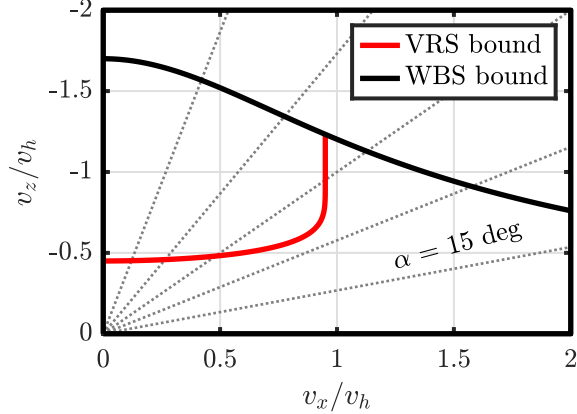
Fig. 6 VRS boundary from [15] and empirical WBS boundary used to predict the onsets of VRS and WBS. The dashed lines are lines of constant shaft angle spaced 15 deg apart; shaft angle increases counterclockwise from 0 deg to 90 deg.

TWS is not explicitly accounted for and is instead considered part of the VRS regime. Based on Eqs. (12) and (13), a rotor is considered to be in VRS (or TWS) when

$$(v_z/v_h)_{\text{WBS}} \leq v_z/v_h < (v_z/v_h)_{\text{VRS}} \tag{14}$$

Similarly, a rotor is considered to be in WBS when

$$v_z/v_h < (v_z/v_h)_{\text{WBS}} \tag{15}$$

Figure 6 depicts these VRS and WBS boundaries.

B. Analysis of Vortex Ring State Measurements

The repeating cycle of vortex ring buildup and separation during VRS leads to reduced thrust and high-amplitude, low-frequency fluctuations in the aerodynamic loads on a rotor. Following [22], the standard deviation (or some multiple thereof) of the low-pass filtered thrust from the TDT is used to quantify the magnitude of the thrust fluctuations in VRS. This statistical approach is especially useful when there is insufficient temporal resolution in the measured low-frequency VRS signals for a rigorous frequency-domain analysis. The choice of the cutoff frequency for the low-pass filter must be high enough to prevent attenuation of the VRS frequencies, but low enough to remove any contributions from the rotor harmonics at 2/rev, 4/rev, etc. and (ideally) the structural modes. The frequencies associated with VRS can be as low as one or two orders of magnitude below the rotor speed; see e.g., [15, 22, 23]. As a result, subsequent developments use a third-order Butterworth low-pass filter (implemented via the `butter` function in MATLAB®) with a 1/rev cutoff frequency. The reduction in thrust is then quantified from the mean of the low-pass filtered rotor loads.

III. Experimental Setup in the Transonic Dynamics Tunnel

This section briefly describes Dragonfly's Phase B* rotor, along with the hardware, measurement transducers, and data acquisition system used during the wind tunnel test campaign in the TDT.

The TDT test campaign measured the performance of a full-scale, flight-like coaxial rotor system (see Fig. 7). The rotor design was primarily driven by requirements derived from the Titan flight environment and planned mission lifetime. Important design drivers included Titan's cryogenic temperatures, minimum fatigue life, frequency separation, and aerodynamic performance. The rotor uses a specific set of airfoils due to their predictable performance across a wide range of Reynolds numbers, high maximum lift coefficient, and benign stall characteristics. The rotors taper from hub to tip with a continuously swept airfoil from the $R/8$ station outboard. The twist and thickness likewise vary from 17.5 deg and 24% chord at the blade root to 6.1 deg and 12% chord at the tip. A smooth, continuous sweep at the hub creates an uninterrupted surface between each rotor blade. The rotor has a diameter of 1.35 m due to constraints associated with packaging four coaxial rotors into Dragonfly's Titan-entry aeroshell. The rotor disk planes in the coaxial pair are spaced a distance $R/2$ apart.

Fig. 7 Flight-like Dragonfly coaxial rotor system installed in the TDT. The depicted coaxial rotor orientation is for a vertical or near-vertical climb condition ($\alpha \approx$ -90 deg). Image courtesy of the Dragonfly TDT Test Team.

The rotor was designed to have a near-infinite fatigue life for the TDT test points and positive safety margins for compliance with TDT safety specifications. Similarly, the rotor was tuned to have a first flap frequency above 90 Hz to provide frequency separation from 4/rev resonances at the 1100 RPM maximum rotor speed used in the TDT.

The rotors are manufactured from monolithic bars of Aluminum 2219-T851 due to this material's excellent, well-characterized fatigue performance at cryogenic temperatures. The manufacturing process involves electron-beam welding aluminum covers onto a rough-machined base, after which the rotor is heat treated to artificially age the welds and machined to the prescribed outer mold line. The finished rotor blades are hollow with rough-machined hub and blade pockets, integral leading-edge spars, and skin thicknesses of approximately 2.5 mm. The machined-out inner pockets facilitate mass optimization and the installation of spin-balance weights. Due to manufacturing constraints, each blade has a span-wise trailing-edge thickness of 0.8 mm. A prescribed surface roughness of 32 µin provides consistent aerodynamic performance between test articles. Small tip vent holes equalize pressure between the blade cavities and the external environment. Each rotor interfaces to the corresponding motor via six 10-32 fasteners in counterbored holes.

Two rotors were tested: an upper counterclockwise spinning rotor and a lower clockwise spinning rotor. The rotors were statically and dynamically spin balanced to less than 0.1 in/s using approximately 100-gram lead weights mounted inside the hub. Each finished rotor weighs approximately 3.7 kg and has a spin-axis moment of inertia of approximately 0.27 kg–m². The fabricated rotors were inspected via dye penetrant testing, ultrasonic scanning, and three-dimensional scanning. Tap testing verified both the as-built flap frequencies and model integrity between test points. Tap test results for the TDT installation indicated that the natural frequencies for the lowest two structural modes were approximately 7.6 Hz (456 RPM) and 8.5 Hz (510 RPM). The third and subsequent modes all had measured natural frequencies in excess of 20 Hz (1200 RPM). An overspeed test spun the rotors at 1320 RPM (120% of the maximum RPM) for five minutes to verify manufacturing quality and structural integrity prior to tunnel entry. Non-destructive testing was then used to verify that the rotors' structural integrity had not significantly degraded during the test campaign.

The test assembly in the TDT consisted of a sting arm, load cells, motors, and the coaxial rotors. The complete assembly was mounted directly to an electronic turntable with a brake/clutch mechanism on the east wall of the TDT. The turntable was used to vary the model's shaft angle from -90 deg to +90 deg (see Fig. 8). The 1.68-m-long sting arm was manufactured from 17-4PH steel; an internal through hole was used to feed electrical harnessing between the tunnel wall and the head assembly. The sting arm's frequency response was tuned to avoid 2/rev and 4/rev resonances within the 500-1100 RPM range. This corresponds to Dragonfly's expected operating RPM range on Titan.

The rotor head assembly included two six-axis ATI Omega 160 load cells, two custom-built KDE motors, and two cooling plates. The load cells were mounted such that each measured the forces and moments transmitted from the corresponding rotor. These loads were proxies for the actual rotor aerodynamic forces and moments. A cooling plate interfaced the motors to the load cells; shop air was passed through the cooling plate to minimize temperature gradients across the load cells. The KDE motors were mounted on top of these cooling plates and provided the interfaces for the rotors. Motor/rotor speeds were measured using optical encoders. Motor power was provided through an external DC power rack connected to 100V/100A ELMO Drum speed controllers.

The test assembly was controlled using a console in the TDT control room. The console communicated via ethernet
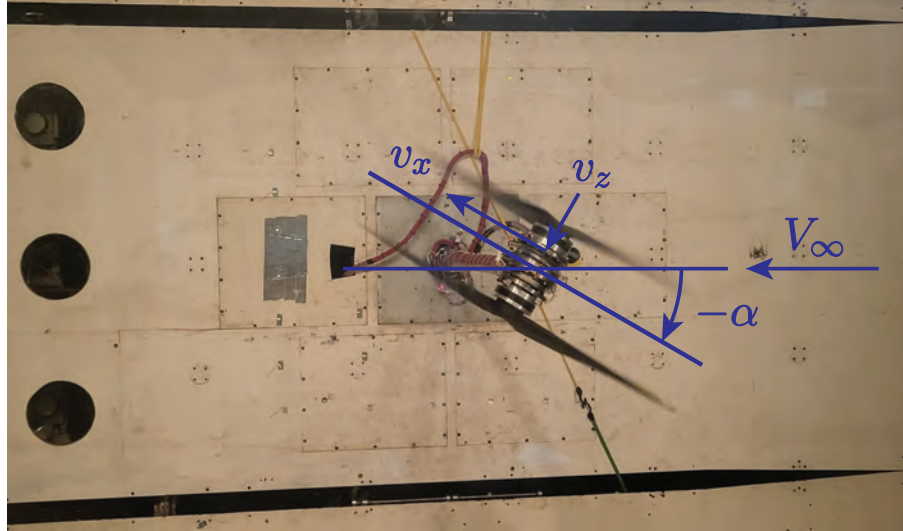
Fig. 8 **The turntable on the TDT's east wall was used to vary the model's shaft angle α from -90 deg to +90 deg. The current configuration corresponds to climb ($\alpha < 0$). Image courtesy of the Dragonfly TDT Test Team.**

to a custom-built data acquisition system located behind the east wall of the test section. A LabView Virtual Instrument controlled model RPM and data acquisition. Data was sampled at 2 kHz; at the maximum rotor speed of 1100 RPM, the load cell measurements were capable of resolving loads with frequency content in excess of 10/rev.

Three parameters were varied during the wind tunnel test: the freestream speed (from 0 m/s to 12 m/s), the shaft angle (from -90 deg to 90 deg), and the rotor RPM (up to 1100 RPM). Most test points were quasi-steady, i.e., the tunnel conditions (freestream speed, temperature, etc.), the shaft angle, and the RPMs on both rotors were all nominally constant during data acquisition. Data was typically acquired for 3 s at each quasi-steady test point. However, data was acquired for at least 20 s at several repeated test points in VRS.

The general operation of the test rig was as follows: For each test point, the sting arm was rotated to the desired shaft angle, the rotors were commanded to 60 RPM, and load cell tares were taken. The rotors were then accelerated to an idle RPM, after which the wind tunnel was accelerated to the desired test speed. Once at the desired test point, the system was commanded through a pre-programmed sequence of velocities, shaft angles, and/or RPMs. At the completion of each test point, the rotors were decelerated to the idle RPM before lowering the wind tunnel speed. Both the upper and lower rotors were commanded to the same nominal RPM at the points considered in this paper.

Figure 9 depicts representative thrust measurements before and after 1/rev low-pass filtering for test points at 6 m/s and 600 RPM. These thrust measurements exclude the first 5 s of recorded data to remove any transients associated with the transition to the commanded operating RPM. In NWS (Figs. 9a–9c), low-pass filtering removes the high-frequency harmonics associated with even multiples of the rotor RPM (e.g., 2/rev, 4/rev, etc.), i.e., it removes any periodicity in the thrust measurements. However, in VRS (Figs. 9d–9f), low-pass filtering reveals a high-amplitude, low-frequency thrust oscillation indicative of vortex formation and breakdown. The dominant VRS frequency visible in the thrust oscillations appears to be on the order of 0.5 Hz, a value comparable to those reported in other studies [15, 22, 23].

The low-pass filter reduces the measurement variance without changing either the mean or the underlying distribution. To see this, Fig. 10 depicts cumulative distribution functions (CDFs) for the coaxial rotor thrust at 6 m/s and 600 RPM in VRS (see Fig. 9f) before and after 1/rev low-pass filtering. The figure specifically compares the empirical CDFs of the original and low-pass filtered thrust signals – evaluated using the MATLAB® function `ecdf` – to the normal distributions evaluated from the corresponding sample means and standard deviations. In doing so, it demonstrates that the measurements both before and after low-pass filtering are approximately normally distributed. Because these results are representative in both NWS and VRS, they provide empirical evidence that supports the use of the sample standard deviation (or some multiple thereof) as a metric for quantifying the amplitude of the unsteady thrust fluctuations in VRS. In what follows, the amplitude of the unsteady thrust fluctuations is defined as twice the corresponding sample standard deviation. As an aside, the sums of the sample means for the forces on the upper and lower rotors are not necessarily equal to the corresponding sample means for the total forces on the coaxial rotor, something that reflects that the normal distributions for the aerodynamic loads on the upper and lower rotors are not independent.
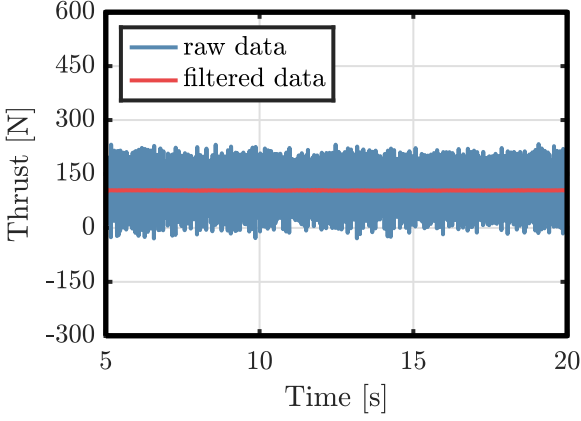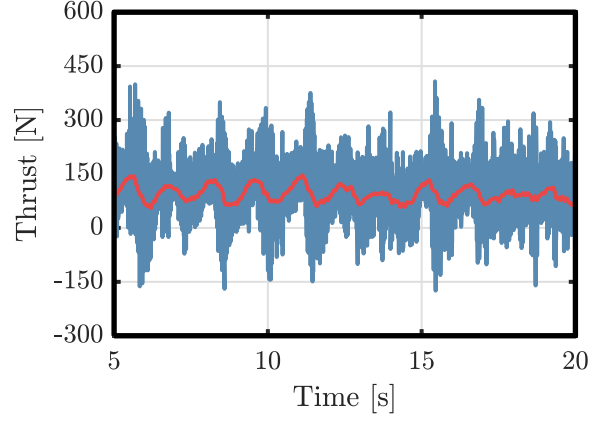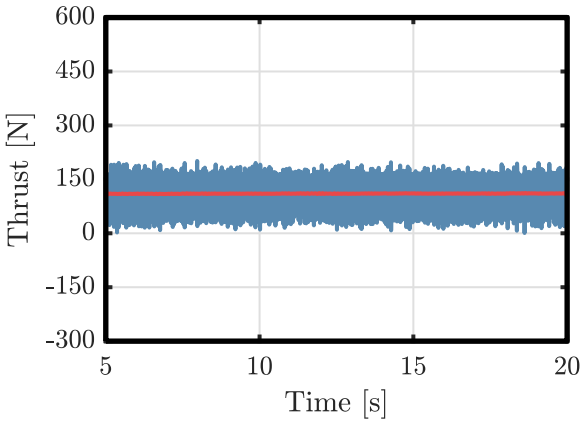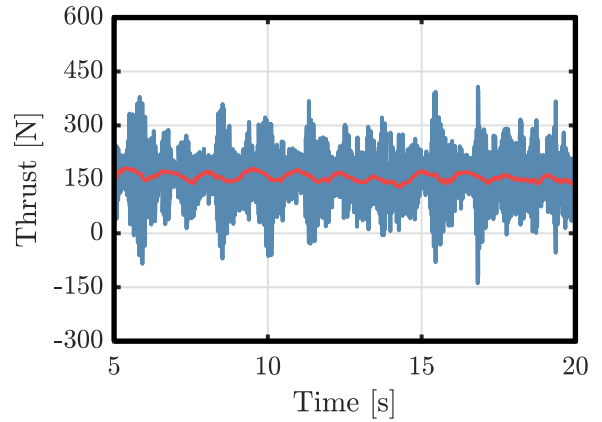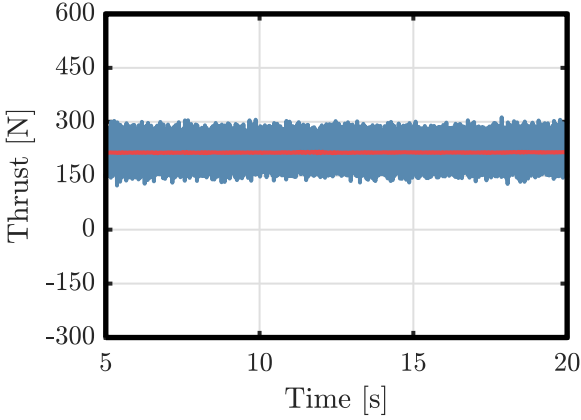
9
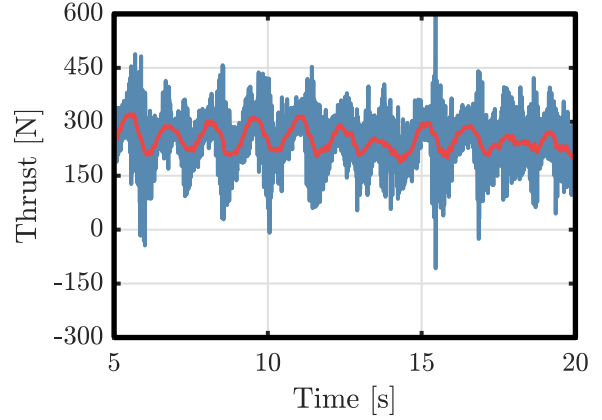
Fig. 9 Representative thrust measurements at V_∞ = 6 m/s and 600 RPM for (a-c) Normal Working State (α = 9 deg) and (d-f) Vortex Ring State (α = 60 deg).

Estimates for the hover thrust, torque, and profile power coefficients were derived from thrust and torque measurements in hover ($V_\infty = 0$) at a range of RPMs (between 600 RPM and 1100 RPM) and shaft angles (between -90 deg and +90 deg). Following Sec. II.A, the thrust and torque coefficients for the upper and lower rotors were derived from quadratic fits of the hover thrust and torque measurements, after which the corresponding coefficients for the coaxial
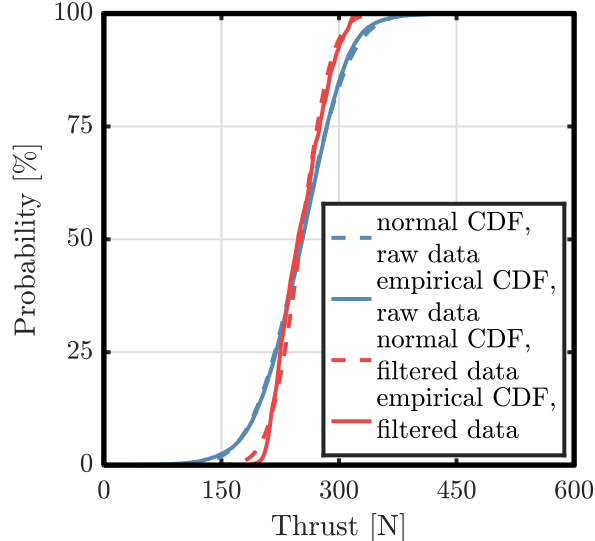
Fig. 10 Representative cumulative distribution functions for unsteady thrust measurements on the coaxial rotor at V_∞ = 6 m/s, α = 60 deg, and 600 RPM in Vortex Ring State.

Table 1 Momentum theory estimates for hover thrust, torque, and profile power coefficients from TDT data

Coefficient	Upper Rotor	Lower Rotor	Coaxial Rotor
C_{T0}	0.00689	0.00468	0.00579
C_{Q0}	-0.00072	0.00057	0.00064
C_{P0}	0.00025	0.00031	0.00029

rotor were evaluated using Eqs. (10) and (11). The corresponding profile power coefficients were then computed using Eq. (9). The resulting estimates for the hover thrust, torque, and profile power coefficients are listed in Table 1. These profile power coefficients are used to calculate induced velocities from the TDT data in Sec. V.

IV. Rotor Performance Analysis using RotCFD

This section provides a brief overview of CFD approaches for modeling rotor performance and describes the RotCFD-based tool used to model Dragonfly's coaxial rotor system in the TDT. RotCFD is widely used to study different rotor configurations (see e.g., [24–26]) and has significant heritage in the development and analysis of Dragonfly's coaxial rotor system [17, 27]. The RotCFD results are compared to data from the TDT in Sec. V.

CFD methods for predicting rotor performance can be subdivided into two categories: blade-modeled and blade-resolved [28, 29]. Figure 11 highlights the tradeoffs between computational cost and model fidelity for several common blade-modeled and blade-resolved CFD approaches. Inherent to the blade-modeled approaches on the left side of Fig. 11 are simplifying assumptions used to reduce the complexity of the blade's local flow physics. These approaches prioritize computational efficiency at the expense of accuracy, making them particularly useful for trade space exploration, flight dynamics modeling, and real-time simulation. In contrast, the blade-resolved approaches on the right side of Fig. 11 solve the Navier-Stokes equations over the true rotor geometry. As a result, they more accurately capture the local flow physics in the vicinity of the blade (provided the blade geometry is discretized with a sufficiently fine mesh). However, this increased accuracy entails a higher computational cost that can be intractable for applications that require a large number of simulations.

Hybrid approaches such as the BEMT-URANS method are practical tools for rotor engineering design and analysis because they balance computational efficiency and accuracy. In this paper, a BEMT-URANS model of Dragonfly's coaxial rotor system is implemented in the rotorcraft CFD analysis software RotCFD [30–32]. The RotCFD implementation of the BEMT-URANS method couples a blade element momentum theory (BEMT) model of the rotor [10] to a
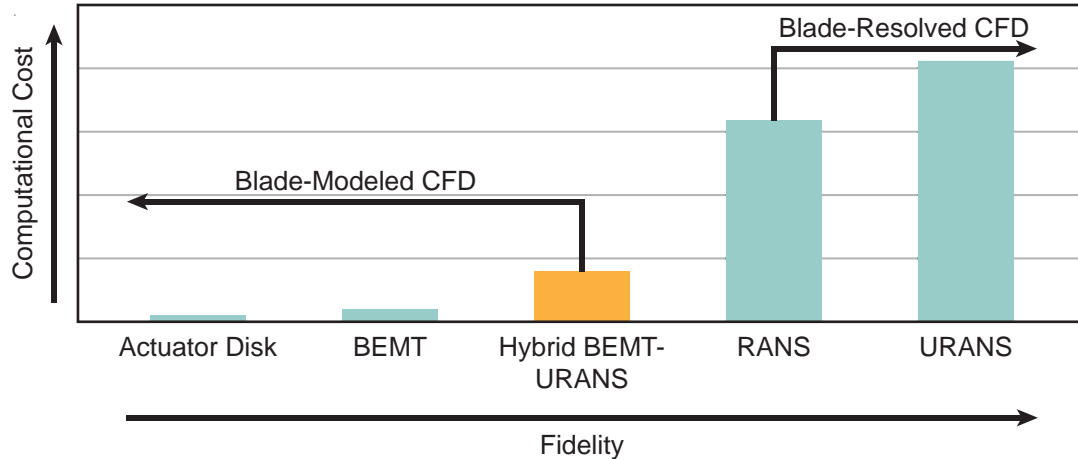
Fig. 11 Relationship between computational cost and model fidelity for various common rotor CFD analysis methods. Figure adapted from [28].

finite-volume structured Cartesian grid solver with implicit time integration for the incompressible unsteady Reynolds-averaged Navier Stokes (URANS) equations, a two-equation k–ϵ turbulence closure model, and the SIMPLE-based solution method [33]. The incompressible URANS equations are sufficient for modeling the global flow field because of the very low inflow and wake velocities (< 20 m/s) relative to the speeds of sound both in R-134a (165 m/s) and on Titan (198 m/s). An actuator disk with distributed momentum sources interfaces the BEMT rotor model and URANS solver. The URANS solver calculates the inflow over the rotor disk; the BEMT rotor model then uses the calculated inflow and C81 airfoil performance lookup tables to resolve the sectional aerodynamic forces and moments on the rotor. Here, the C81 tables are derived from compressible two-dimensional airfoil CFD simulations in OVERFLOW [34] with the Spalart-Allmaras turbulence closure model [35]. The aerodynamic forces and moments are time-averaged to reduce computational cost while retaining effects due to essential flow physics, e.g., retreating blade stall and advancing blade compressibility†, and then fed back to the URANS flow field through the distributed momentum sources in the actuator disk. The URANS solution for the global flow field more accurately models both the rotor inflow and wake trajectory than simpler blade-modeled approaches. This allows the BEMT-URANS approach to analyze rotor flow states such as VRS that are typically considered too complicated for blade-modeled approaches. The RotCFD model of Dragonfly's coaxial rotor system is GPU accelerated and implemented in a high-performance computing environment to achieve a significant reduction in computational time compared to blade-resolved CFD; for additional details, see [28].
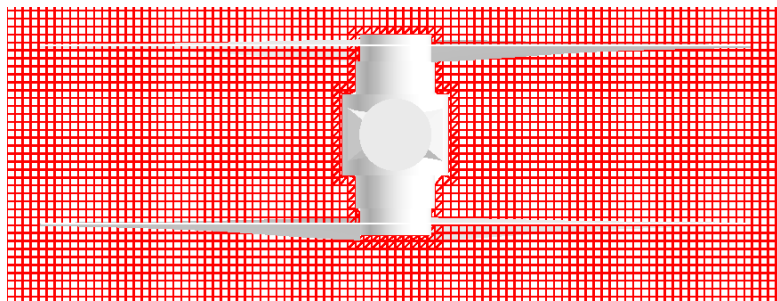
Fig. 12 RotCFD model of the TDT test assembly. The sting arm that attaches the coaxial rotor system to the wall of the TDT points out of the page.

The BEMT-URANS approach can also model both rotor-rotor and rotor-body interactions. RotCFD specifically uses tetrahedral body-fitted cells to discretize solid bodies such as rotor hubs and airframes in the URANS solver.

---

†Even though the URANS equations are incompressible, advancing blade compressibility effects are still captured in the BEMT model through the use of C81 tables derived from compressible CFD simulations.

These tetrahedral cells are used to model the rotor hubs, motors, and sting arm in the RotCFD model of the TDT test assembly (see Fig. 12). Because these cells are typically insufficiently refined to develop the boundary layer on a solid body, boundary-layer effects are instead modeled using wall functions. Despite the use of wall functions, RotCFD has been shown to accurately capture the bluff-body aerodynamic effects important for rotor-airframe interactions [31].

A grid convergence study was used to verify the RotCFD model of the TDT test assembly. The grid convergence study specifically varied the number of cells across the rotor disk and the sizes of the refinement regions to quantify the relationship between the grid size and the disk-integrated forces and moments. The results indicated that the disk-integrated forces and moments converged with approximately 90 cells spanning the rotor diameter. This result is in good agreement with those from similar studies with BEMT-URANS flow solvers; see e.g., [36].

Table 2   RotCFD estimates for hover thrust, torque, and profile power coefficients

Coefficient	Coaxial, R-134a			Coaxial, Titan			Isolated Rotor, R-134a	
	Upper	Lower	Coaxial	Upper	Lower	Coaxial	Upper	Lower
C_{T0}	0.00737	0.00502	0.00619	0.00748	0.00478	0.00613	0.00755	0.00737
C_{Q0}	-0.00070	0.00057	0.00064	-0.00066	0.00055	0.00061	-0.00071	0.00069
C_{P0}	0.00018	0.00029	0.00024	0.00014	0.00028	0.00022	0.00018	0.00018

Several thousand RotCFD runs were used to generate tables of the aerodynamic forces and moments on Dragonfly's coaxial rotor system throughout its expected flight envelope (freestream speeds between 0 m/s‡ and 10.5 m/s, shaft angles between -90 deg and 90 deg, and rotor speeds between 100 and 1250 RPM) in both R-134a and Titan conditions. The flight envelope was discretized using step sizes of approximately 1.5 m/s, 15 deg, and 100 RPM. The RotCFD runs specifically considered three configurations: the coaxial rotor system with both rotors at the same RPM, the isolated upper rotor (lower rotor unmodeled), and the isolated lower rotor (upper rotor unmodeled). Table 2 lists the corresponding hover thrust, torque, and profile power coefficients [calculated from Eq. (9)]. These coefficients show generally good agreement with their experimentally derived counterparts in Table 1 and are subsequently used to normalize RotCFD results in Sec. V. The runs for the isolated upper and lower rotors are particularly useful for quantifying the performance differences between the isolated and coaxial rotors, e.g., those due to rotor-rotor interaction. The isolated upper and lower rotors have nearly identical performance, but small differences exist due to relative differences in the test assembly geometry. This is apparent from the small discrepancies between the corresponding hover thrust and torque coefficients in Table 2.

This paper is only concerned with the RotCFD rotor performance predictions for axial flight. The R-134a rotor performance table facilitates comparisons with the TDT test results (Sec. V.A) and between coaxial and isolated rotors (Sec. V.B); the Titan rotor performance table then helps extrapolate the TDT results to Titan conditions (Sec. V.D).

V. Results and Discussion

This section studies the performance of Dragonfly's Phase B* coaxial rotor system in VRS using RotCFD and results from the TDT. Sec. V.A specifically compares the thrust and torque predictions in axial flight from RotCFD with the corresponding measurements from the TDT. To better understand how the coaxial rotor behaves in VRS, Sec. V.B uses RotCFD predictions to compare the performance of the coaxial rotor to an analogous isolated rotor. Sec. V.C then uses TDT data to quantify the magnitude of the thrust fluctuations in VRS. Finally, Sec. V.D uses RotCFD predictions for the Titan environment to provide insights into how VRS may ultimately affect the Dragonfly lander.

A. Comparisons between RotCFD and Experiment

To build confidence in the RotCFD model, Fig. 13 compares the RotCFD predictions for the thrust and torque coefficients in axial flight with those from the measurements in the TDT. The thrust and torque coefficients in these and subsequent figures span the range of freestream speeds and rotor RPMs and are plotted as functions of the axial advance ratio $\mu_z = v_z/(\Omega R)$. The TDT measurements show significant scatter, especially for the upper rotor and points in VRS, i.e., for $-0.15 \leq \mu_z \leq -0.05$. This leads to often poor point-wise agreement between RotCFD and the TDT in descent ($\mu_z < 0$). This point-wise agreement is significantly improved in hover and climb ($\mu_z \geq 0$). At the macroscale,

---
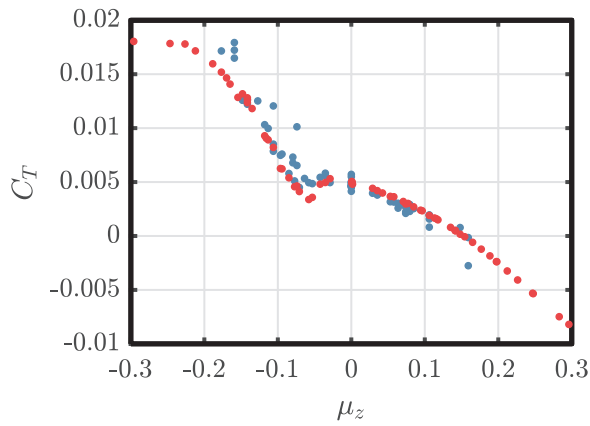
‡To improve numerical convergence, hover cases were actually run with a small axial climb velocity of 0.05 m/s.
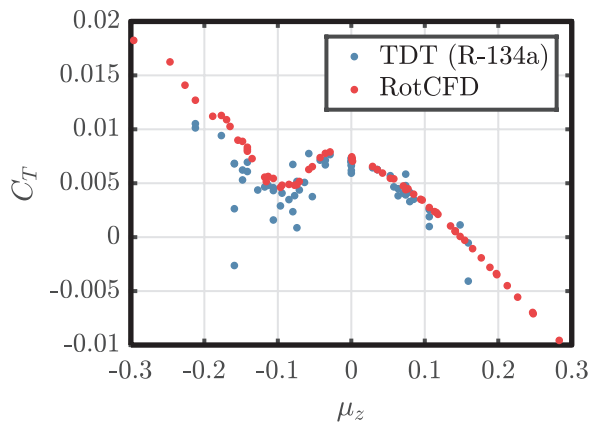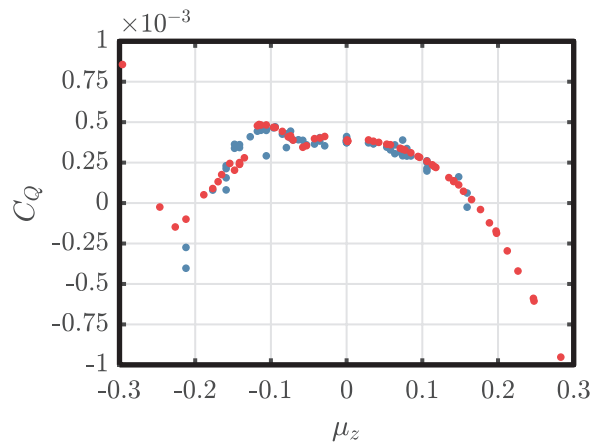
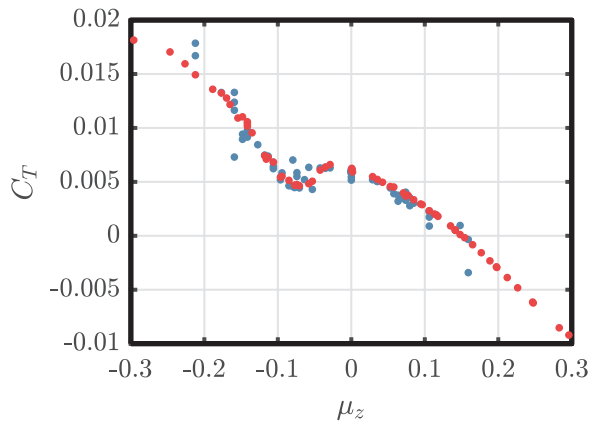**(a) upper rotor thrust coefficients**
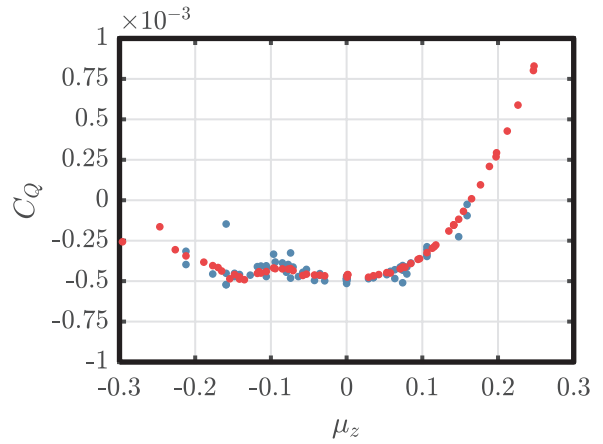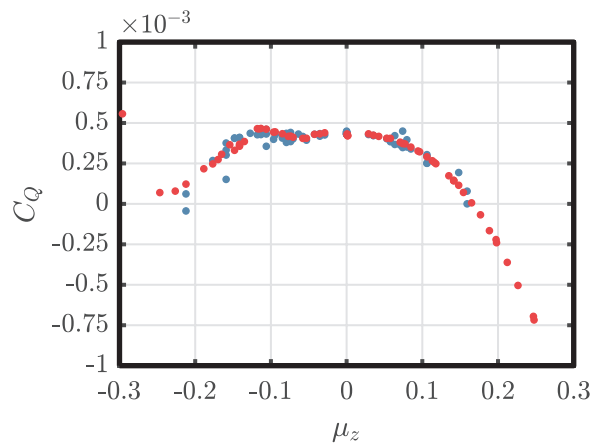
(b) lower rotor thrust coefficients

(c) coaxial rotor thrust coefficients
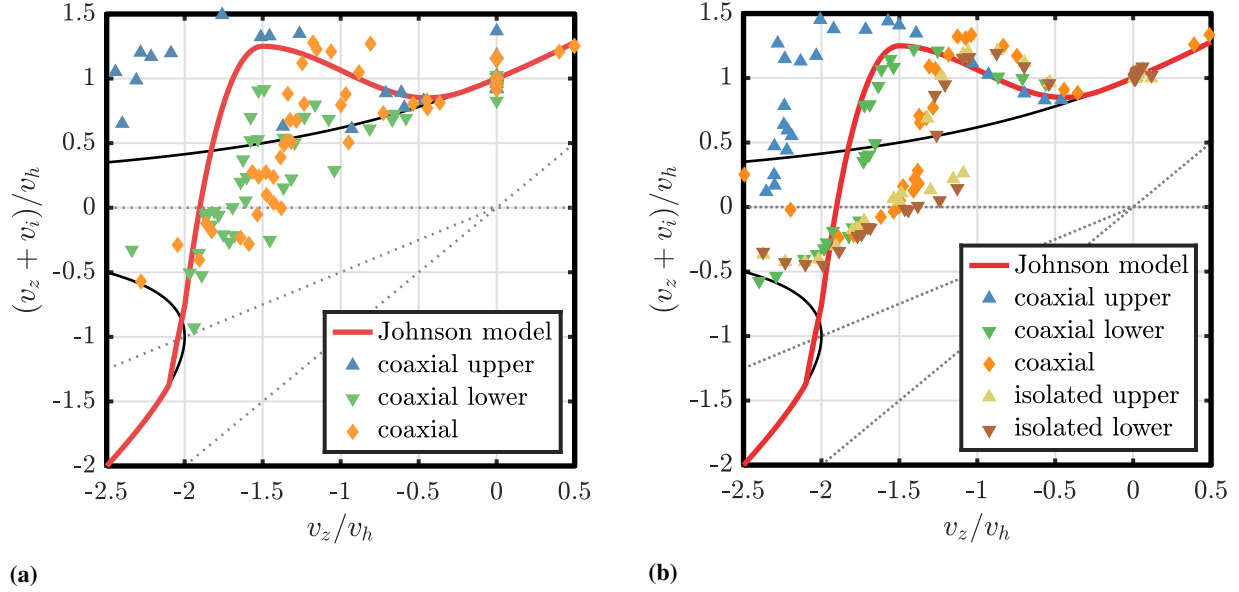
(d) upper rotor torque coefficients

(e) lower rotor torque coefficients

(f) coaxial rotor torque coefficients

Fig. 13   Comparison of (a-c) thrust and (d-f) torque coefficients from the TDT and RotCFD for the upper, lower, and coaxial rotors in axial flight.

14

Fig. 14 Comparison of the Johnson VRS model for axial flight ($v_x = 0$) with the induced velocities (a) on the upper rotor, lower rotor, and coaxial rotor from the TDT and (b) on the upper rotor, lower rotor, coaxial rotor, and isolated upper and lower rotors from RotCFD.

RotCFD and the TDT show similar trends across the range of considered flight conditions and exhibit generally good agreement in the sense that the RotCFD results are reasonable fits to the scatter in the TDT data.

Figure 14a then compares the mean induced velocities from the TDT with the Johnson model. The TDT measurements again show significant scatter, especially for the upper rotor. This scatter may be due to the lower rotor shielding the upper rotor from the effects of VRS. Despite this, the lower and coaxial rotors are still qualitatively similar to the Johnson model, i.e., they show the same general trends but poor point-wise agreement. As a result, the Johnson model appears to be a good indicator of VRS for the lower rotor and the coaxial pair.

B. Comparisons between Single and Coaxial Rotors

Following [19], the coaxial rotor's performance in VRS is compared to the performance of isolated rotors with the same design as the coaxial rotor to better understand how the coaxial rotor behaves in VRS. The caveat is that the performance of a rotor in VRS is often strongly influenced by its geometry [23], which for a coaxial rotor includes the spacing between its rotor disk planes. For this reason, even though these results may have general implications for rotor design, they are to be interpreted as specific to Dragonfly's Phase B* coaxial rotor system.

Figures 15a and 15b compare the thrust and torque coefficient predictions from RotCFD for the coaxial rotor in axial flight with those from isolated upper and lower rotors. The figure also reports the thrust and torque coefficients on the upper and lower rotors in the coaxial pair. The coefficients are normalized relative to the corresponding hover coefficients from Table 2 to better highlight the reductions in thrust and torque that occur during VRS.

In hover and climb ($\mu_z \geq 0$), all five curves in Figs. 15a and 15b collapse to a single branch. This suggests that the coaxial rotor behaves like an isolated rotor in these flight conditions despite the differing numerical values for the thrusts and torques. In contrast, the five curves separate into distinct branches in descent ($\mu_z < 0$). Each curve shows qualitatively similar behavior in VRS and the subsequent transition into TWS. In particular, there is an initial reduction in thrust and torque at the low-to-moderate negative values of μ_z characteristic of VRS; the thrust and torque then increase as the rotor transitions from VRS into TWS. From there, the thrust continues to increase as μ_z decreases, whereas the torque begins to decrease as the rotor moves from TWS to WBS. The transition from TWS to WBS occurs when $C_Q = 0$; hence, Fig. 15b shows several points in WBS.

Figures 15a and 15b likewise show that the isolated rotors begin experiencing thrust and torque reductions at lower negative values of μ_z than the coaxial rotor. The isolated rotors similarly see smaller peak thrust and torque reductions that begin to recover at lower negative values of μ_z than the coaxial rotor. In other words, when compared to the

15
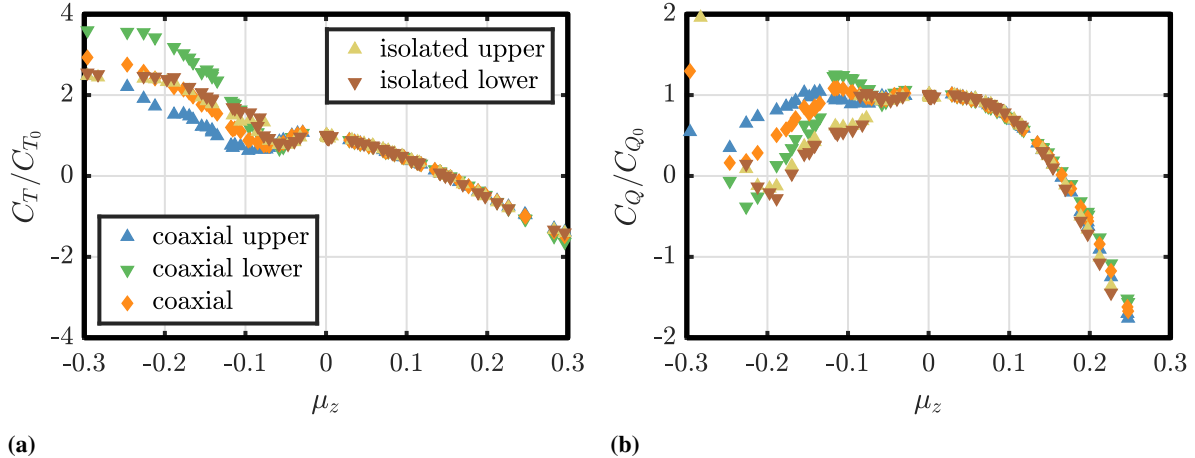
Fig. 15 Comparison of RotCFD (a) thrust and (b) torque coefficient predictions for the upper rotor, lower rotor, coaxial rotor, and isolated upper and lower rotors in axial flight.

analogous isolated rotors, the coaxial rotor experiences larger thrust and torque reductions over a wider range of μ_z. However, the initial thrust and torque reductions occur at higher negative values of μ_z; a similar result has been reported in [19]. These results suggest that the coaxial rotor is potentially more robust to the onset of VRS than an isolated rotor. Importantly, the figures also demonstrate that the lower rotor in the coaxial pair enters and recovers from VRS at greater, i.e., less-negative, values of μ_z than the upper rotor. Because the upper rotor experiences thrust and torque reductions over a larger range of μ_z, these results seem to indicate that rotor-rotor interactions are important contributors to the performance of the upper rotor, and by extension, the coaxial rotor, in VRS.

Figure 14b then overlays the induced velocity predictions for axial flight from RotCFD for both the coaxial and isolated upper and lower rotors onto the Johnson model. The curves are again qualitatively similar in that they tend to have the same basic shape as the Johnson model, i.e., they depict similar behaviors in VRS and rejoin the momentum theory solution for small normalized descent rates (e.g., for $v_z/v_h > -0.5$). The curves are also broadly similar to the TDT results in Fig. 14a; the induced velocities for the lower rotor specifically show excellent agreement with both the Johnson model and the corresponding TDT test points in Fig. 14a. This suggests that the Johnson model may be an excellent predictor of VRS for the lower rotor in particular, although additional work is necessary to determine if this result is generally true across the flight envelope, i.e., for $v_x/v_h > 0$. Similar to the TDT results in Fig. 14a, the RotCFD results in Fig. 14b do not rejoin the momentum theory solution for WBS at high descent rates (i.e., for $v_z/v_h < -2$).

## C. Measured Thrust Fluctuations in Vortex Ring State

The TDT measurements are used to quantify the amplitude of the unsteady thrust fluctuations in VRS. Figure 16 overlays the unsteady thrust fluctuations (defined as two sample standard deviations and reported as percentages relative to the mean) and the corresponding mean thrust coefficients (normalized relative to the hover thrust coefficients from Table 1) onto the VRS boundary from Fig. 6. Figure 16 only includes test points at 600 RPM and 750 RPM.

There are several important takeaways from Figs. 16a–16c. First, the thrust fluctuations outside of VRS are small (less than 10%, and often less than 5%). At 600 RPM, the 1/rev low-pass filter does not attenuate the test assembly's 7.6 Hz (456 RPM) and 8.5 Hz (510 RPM) vibration modes. Because the thrust fluctuations are derived from load cells that measure the total rotor loads, i.e., the aerodynamic and inertial loads, aero-mechanical vibrations are a possible source of the measured unsteadiness outside VRS (and a possible contributor to the unsteadiness inside VRS). Second, the VRS with the largest thrust fluctuations occurs in steep descents with $\alpha > 60$ deg and $-1.25 < v_z/v_h < -0.75$. The thrust fluctuations rapidly decrease outside of this region. In particular, there is minimal unsteadiness for $\alpha < 45$ deg, irrespective of descent speed. This implies that Dragonfly may be able to safely operate in high speed descending forward flight, at least as far as VRS is concerned. This has important ramifications for extending Dragonfly's range on Titan. Third, the largest unsteady thrust fluctuations occur on the upper rotor. This is likely the result of rotor-rotor interactions, e.g., vortex rings from the lower rotor interacting with the upper rotor. Finally, the unsteadiness decreases as the descent rate increases and approaches the WBS boundary [Eq. (13)]. Together, these results suggest that the
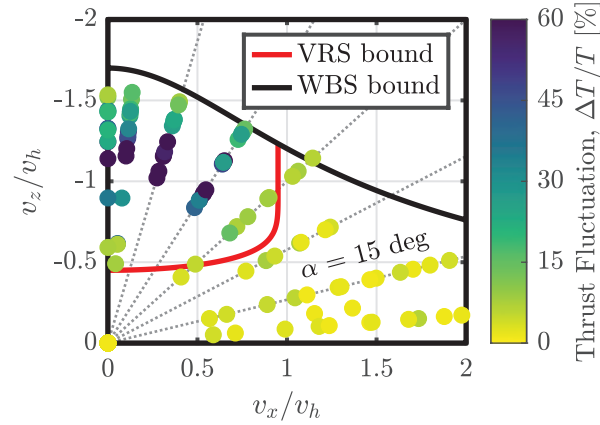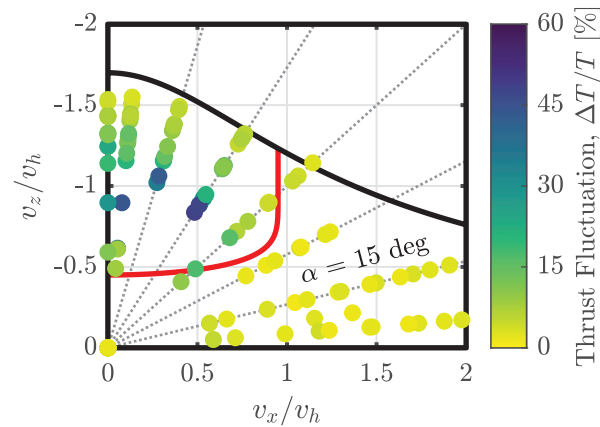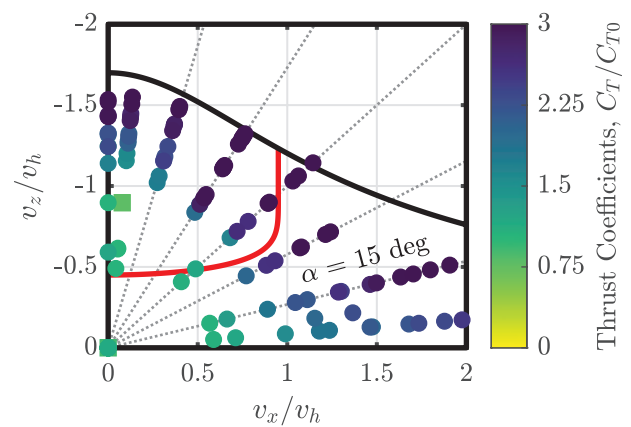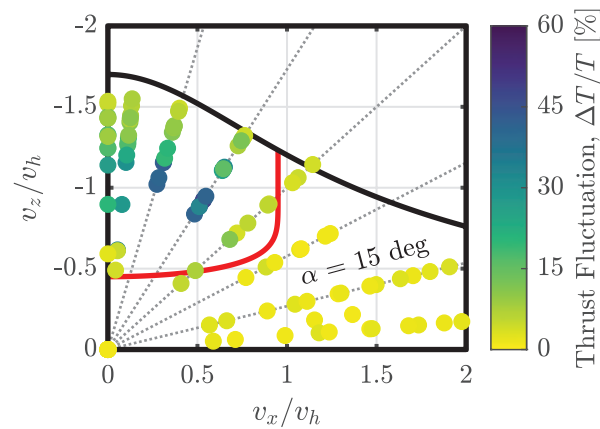
(a) upper rotor thrust fluctuations
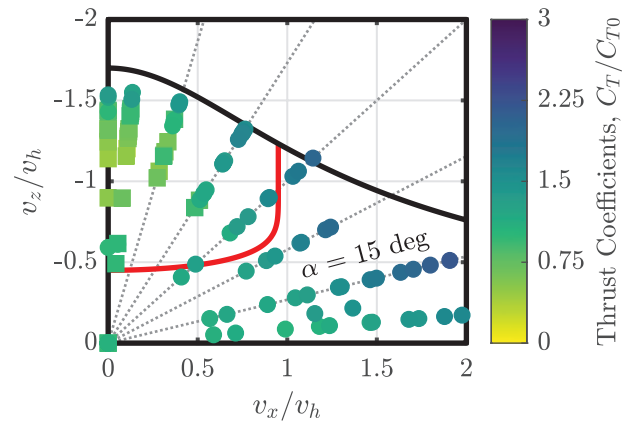
(b) lower rotor thrust fluctuations

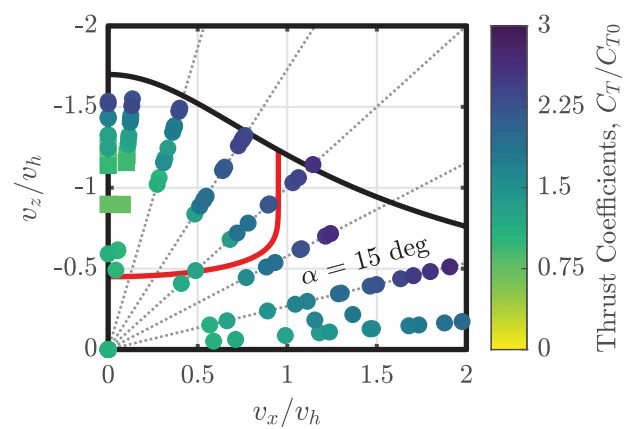**(c) coaxial rotor thrust fluctuations**

(d) upper rotor thrust coefficients

(e) lower rotor thrust coefficients

(f) coaxial rotor thrust coefficients

Fig. 16   Unsteady thrust fluctuations relative to the mean (a-c) and thrust coefficients normalized relative to hover (d-f) for quasi-steady test points at 600 RPM and 750 RPM. In (d-f), the square symbols denote points where $C_T/C_{T0} < 1$. The dashed lines are lines of constant shaft angle spaced 15 deg apart; shaft angle increases counterclockwise from 0 deg to 90 deg.

17

Johnson VRS boundary may be conservative in that it appears to overpredict the size of the flight envelope susceptible to strong VRS, at least for the considered RPM range.

The mean thrust coefficients relative to hover in Figs. 16d–16f exhibit comparable trends to those in Fig. 15a, namely that the thrust decreases in VRS and then recovers as v_z/v_h approaches the WBS boundary. However, as the forward flight speed increases, i.e., as v_x/v_h increases, so too does the minimum C_T/C_{T0}. For the coaxial rotor in particular, C_T/C_{T0} only decreases below 1 in steep descents with small forward flight speeds ($\alpha > 75$ deg). For these reasons, Figs. 16d–16f suggest that the unsteady aerodynamic loads in VRS likely have a more significant effect on vehicle dynamics than the corresponding thrust reduction.

D. Extrapolation to Titan Conditions

All of the results presented so far are for the coaxial rotor system in R-134a. These final results compare the performance of the coaxial rotor system in R-134a and Titan conditions.

Figure 17 specifically compares the RotCFD thrust and torque coefficient predictions for axial flight in both R-134a and Titan conditions. The thrust and torque coefficients show generally good agreement between R-134a and Titan with small discrepancies in climb and larger ones in descent. These discrepancies are slightly more pronounced in the torque coefficient plots. However, the most significant takeaways from Fig. 17 are related to rotor performance in VRS. Figures 17c and 17f specifically suggest that if anything, there may be marginally larger thrust and torque reductions over a slightly wider range of μ_z on Titan than in R-134a. Figure 17 also demonstrates that the thrust and torque reductions in VRS on Titan are larger for the upper rotor than the lower one, in line with the observations in Secs. V.B and V.C. Finally, Fig. 17 indicates that the thrust and torque scale approximately linearly with density between R-134a and Titan conditions, irrespective of the rotor's working state.
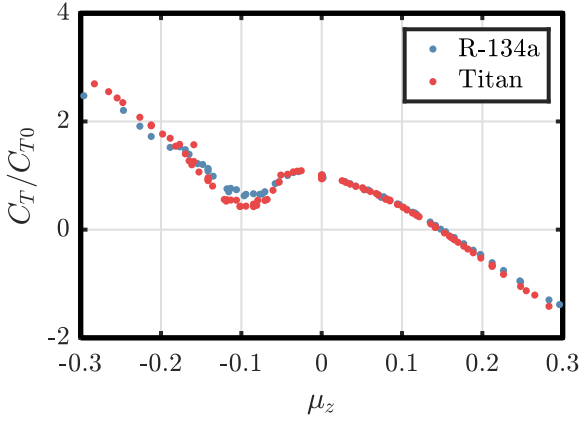
VI. Conclusion

This paper has studied the performance of the Dragonfly relocatable rotorcraft lander's Phase B* coaxial rotor system in vortex ring state (VRS) using both computational fluid dynamics (CFD) and measurements in a Titan-surrogate environment (R-134a) from a recent wind tunnel test campaign in the Transonic Dynamics Tunnel (TDT) at NASA's Langley Research Center.

A GPU-accelerated CFD tool for calculating rotor performance has been developed using the BEMT-URANS method in the commercial CFD software RotCFD. This CFD tool has been subsequently validated against rotor aerodynamic load measurements from the TDT. In particular, it was shown that there is good overall agreement between the rotor performance predictions from RotCFD and the measurements from the TDT, at least for the considered range of conditions in axial (vertical) flight. The RotCFD tool was then used to compare the coaxial rotor's performance (i) relative to analogous isolated rotors and (ii) in R-134a and the Titan environment.
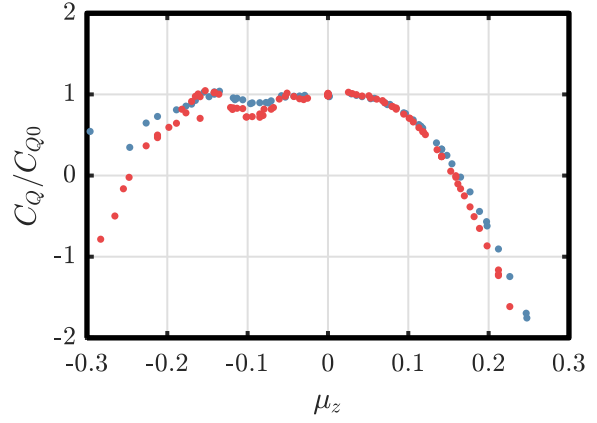
The analysis demonstrated that there is good overall agreement between the Johnson VRS model and both the TDT and RotCFD results. This agreement is better for both the lower rotor and the coaxial rotor than it is for the upper rotor. The analysis likewise demonstrated that the effects of VRS, namely the mean thrust and torque reductions and the unsteadiness in the aerodynamic loads, tend to be larger on the upper rotor than the lower rotor. Additionally, the upper rotor tends to experience VRS at higher descent rates than the lower rotor. It was theorized that these behaviors are at least partially attributable to rotor-rotor interactions, e.g., vortex rings from the lower rotor interacting with the upper rotor. Similarly, the mean thrust and torque reductions in VRS were predicted to be comparable in R-134a and the Titan environment. Finally, performance comparisons between the coaxial rotor and isolated rotors with the same design as the coaxial rotor suggested that the coaxial rotor may be more robust to the onset of VRS, i.e., VRS may start at higher descent rates. However, the results also suggest that the subsequent VRS effects may result in larger thrust reductions that occur over a wider range of descent rates. The caveat is that these results are specific to Dragonfly's Phase B* coaxial rotor system. Extrapolating these results to other coaxial rotor systems requires a more detailed understanding of the interaction between a coaxial rotor system's design and its VRS performance. This is left to future work.
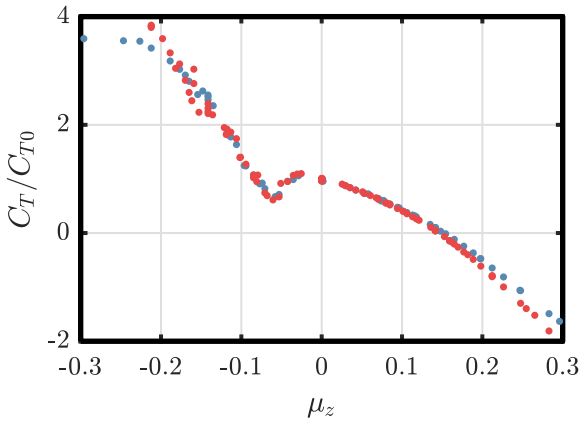
(a) upper rotor thrust coefficients

(b) lower rotor thrust coefficients
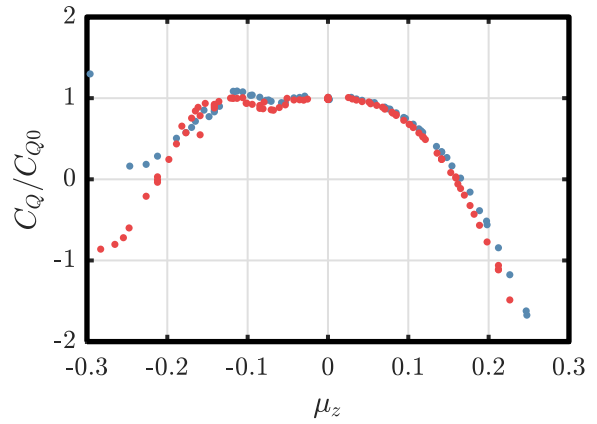
(c) coaxial rotor thrust coefficients

(d) upper rotor torque coefficients
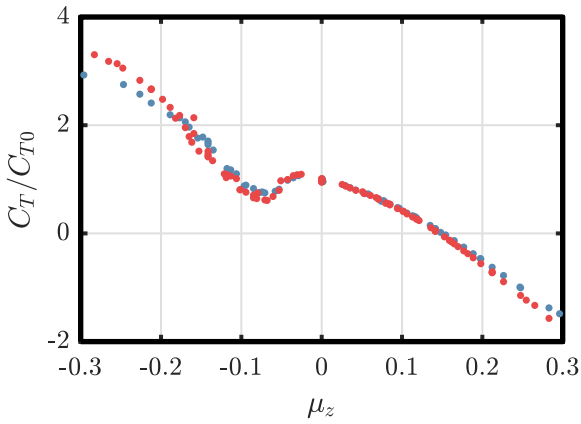
(e) lower rotor torque coefficients

(f) coaxial rotor torque coefficients

Fig. 17   Comparison of RotCFD thrust and torque coefficient predictions for axial flight in R-134a and Titan conditions.

References

[1] Lorenz, R. D., Turtle, E. P., Barnes, J. W., Trainer, M. G., Adams, D. S., Hibbard, K. E., Sheldon, C. Z., Zacny, K., Peplowski, P. N., Lawrence, D. J., Ravine, M. A., McGee, T. G., Sotzen, K. S., MacKenzie, S. M., Langelaan, J. W., Schmitz, S., Wolfarth, L. S., and Bedini, P. D., "Dragonfly: A Rotorcraft Lander Concept for Scientific Exploration at Titan," *Johns Hopkins APL Technical Digest*, Vol. 34, No. 3, 2018, pp. 374–387.

[2] Barnes, J. W., Turtle, E. P., Trainer, M. G., Lorenz, R. D., MacKenzie, S. M., Brinckerhoff, W. B., Cable, M. L., Ernst, C. M., Freissinet, C., Hand, K. P., Hayes, A. G., Hörst, S. M., Johnson, J. R., Karkoschka, E., Lawrence, D. J., Le Gall, A., Lora, J. M., McKay, C. P., Miller, R. S., Murchie, S. L., Neish, C. D., Newman, C. E., Núñez, J., Panning, M. P., Parsons, A. M., Peplowski, P. N., Quick, L. C., Radebaugh, J., Rafkin, S. C. R., Shiraishi, H., Soderblom, J. M., Sotzen, K. S., Stickle, A. M., Stofan, E. R., Szopa, C., Tokano, T., Wagner, T., Wilson, C., Yingst, R. A., Zacny, K., and Stähler, S. C., "Science Goals and Objectives for the Dragonfly Titan Rotorcraft Relocatable Lander," *The Planetary Science Journal*, Vol. 2, No. 4, 2021, p. 130. doi:https://doi.org/10.3847/PSJ/abfdcf.

[3] Lorenz, R. D., "Flight Power Scaling of Airplanes, Airships, and Helicopters: Application to Planetary Exploration," *Journal of Aircraft*, Vol. 38, No. 2, 2001, pp. 208–214. doi:https://doi.org/10.2514/2.2769.

[4] Langelaan, J. W., Schmitz, S., Palacios, J., and Lorenz, R. D., "Energetics of rotary-wing exploration of Titan," *IEEE Aerospace Conference*, Big Sky, Montana, 2017. doi:https://doi.org/10.1109/AERO.2017.7943650.

[5] Opazo, T. I., Zahirudin, R. A. R., Palacios, J., Schmitz, S., and Langelaan, J. W., "Analytical and Experimental Power Minimization for Fixed-Pitch Coaxial Rotors in Hover," *Journal of Aircraft*, Vol. 60, No. 2, 2023, pp. 546–559. doi:https://doi.org/10.2514/1.C036807.

[6] Newman, S., Brown, R., Perry, J., Lewis, S., Orchard, M., and Modha, A., "Predicting the Onset of Wake Breakdown for Rotors in Descending Flight," *Journal of the American Helicopter Society*, Vol. 48, No. 1, 2003, pp. 28–38. doi:https://doi.org/10.4050/JAHS.48.28.

[7] Brand, A., Dreier, M., Kisor, R., and Wood, T., "The Nature of Vortex Ring State," *Journal of the American Helicopter Society*, Vol. 56, No. 2, 2011, p. 22001. doi:https://doi.org/10.4050/JAHS.56.022001.

[8] Veismann, M., Yos, D., and Gharib, M., "Parametric study of small-scale rotors in axial descent," *Physics of Fluids*, Vol. 34, No. 3, 2022, p. 035124. doi:https://doi.org/10.1063/5.0083761.

[9] Brown, R. E., "Are eVTOL Aircraft inherently more susceptible to the Vortex Ring State than Conventional Helicopters?" *48th European Rotorcraft Forum*, Winterthur, Switzerland, 2022.

[10] Johnson, W., *Rotorcraft Aeromechanics*, Cambridge University Press, New York, New York, 2013. doi:https://doi.org/10.1017/CBO9781139235655.

[11] Tritschler, J. K., Celi, R., and Leishman, J. G., "Methodology for Rotorcraft Brownout Mitigation Through Flight Path Optimization," *Journal of Guidance, Control, and Dynamics*, Vol. 37, No. 5, 2014, pp. 1524–1538. doi:https://doi.org/10.2514/1.G000330.

[12] Talaeizadeh, A., Nejat Pishkenari, H., and Alasty, A., "Quadcopter Fast Pure Descent Maneuver Avoiding Vortex Ring State Using Yaw-Rate Control Scheme," *IEEE Robotics and Automation Letters*, Vol. 6, No. 2, 2021, pp. 927–934. doi:https://doi.org/10.1109/LRA.2021.3052436.

[13] Wang, Y., Li, A., Tian, H., and Yang, S., "Vortex Ring State Avoidance Control Scheme Design for Nonlinear Autonomous Helicopter," *Journal of Guidance, Control, and Dynamics*, Vol. 45, No. 8, 2022, pp. 1546–1553. doi:https://doi.org/10.2514/1.G006682.

[14] Wolkovitch, J., "Analytical Prediction of Vortex-Ring Boundaries for Helicopters in Steep Descents," *Journal of the American Helicopter Society*, Vol. 17, No. 3, 1972, pp. 13–19. doi:https://doi.org/10.4050/JAHS.17.13.

[15] Johnson, W., "Model for Vortex Ring State Influence on Rotorcraft Flight Dynamics," Tech. Rep. NASA/TP-2005-213477, NASA Ames Research Center, Moffett Field, California, December 2005.

[16] Basset, P., Chen, C., Prasad, J. V. R., and Kolb, S., "Prediction of Vortex Ring State Boundary of a Helicopter in Descending Flight by Simulation," *Journal of the American Helicopter Society*, Vol. 53, No. 2, 2008, pp. 139–151. doi:https://doi.org/10.4050/JAHS.53.139.

[17] Cornelius, J., Opazo, T., Schmitz, S., Langelaan, J., Villac, B., Adams, D., Rodovskiy, L., and Young, L., "Dragonfly — Aerodynamics during Transition to Powered Flight," *77th Annual Vertical Flight Society Forum & Technology Display*, Virtual Event, 2021.

[18] Boss, C., and Rodovskiy, L., "From Freefall to Controlled Descent: Dragonfly's Transition to Powered Flight," *2023 AAS/AIAA Astrodynamics Specialist Conference*, Big Sky, Montana, 2023.

[19] Kinzel, M. P., Cornelius, J. K., Schmitz, S., Palacios, J. L., Langelaan, J. W., Adams, D., and Lorenz, R., "An Investigation of the Behavior of a Coaxial Rotor in Descent and Ground Effect," *AIAA SciTech Forum*, San Diego, California, 2019. doi:https://doi.org/10.2514/6.2019-1098, AIAA 2019-1098.

[20] Yan, S., Getz, D. V., Palacios, J., Kinzel, M., Schmitz, S., and Langelaan, J., "Design, Fabrication and Preliminary Testing of an Experimental Measurement Rig for Co-Axial Rotors," *AIAA SciTech Forum*, San Diego, California, 2019. doi:https://doi.org/10.2514/6.2019-1096, AIAA 2019-1096.

[21] Feil, R., Rauleder, J., Cameron, C. G., and Sirohi, J., "Aeromechanics Analysis of a High-Advance-Ratio Lift-Offset Coaxial Rotor System," *Journal of Aircraft*, Vol. 56, No. 1, 2019, pp. 166–178. doi:https://doi.org/10.2514/1.C034748.

[22] Foster, J. V., and Hartman, D., "High-Fidelity Multi-Rotor Unmanned Aircraft System (UAS) Simulation Development for Trajectory Prediction Under Off-Nominal Flight Dynamics," *AIAA Aviation Forum*, Denver, Colorado, 2017. doi:https://doi.org/10.2514/6.2017-3271, AIAA 2017-3271.

[23] Stack, J., Caradonna, F. X., and Savaş, Ö., "Flow Visualizations and Extended Thrust Time Histories of Rotor Vortex Wakes in Descent," *Journal of the American Helicopter Society*, Vol. 50, No. 3, 2005, pp. 279–288. doi:https://doi.org/10.4050/1.3092864.

[24] Koning, W. J. F., Russell, C. R., Solis, E., and Theodore, C., "Mid-Fidelity Computational Fluid Dynamics Analysis of the Elytron 4S UAV Concept," Tech. Rep. NASA/TM-2018-219788, NASA Ames Research Center, Moffett Field, California, November 2018.

[25] Conley, S., Russell, C., Kallstrom, K., Koning, W., and Romander, E., "Comparing RotCFD Predictions of the Multirotor Test Bed with Experimental Results," *76th Annual Vertical Flight Society Forum & Technology Display*, Virtual Event, 2020.

[26] Conley, S., and Shirazi, D., "Comparing Simulation Results from CHARM and RotCFD to the Multirotor Test Bed Experimental Data," *AIAA Aviation Forum*, Virtual Event, 2021. doi:https://doi.org/10.2514/6.2021-2540, AIAA 2021-2540.

[27] Cornelius, J., and Schmitz, S., "Rotor Performance Predictions for UAM — Single vs Coaxial Rigid Rotors," *Aeromechanics for Advanced Vertical Flight Technical Meeting*, San Jose, California, 2022.

[28] Cornelius, J. K., and Schmitz, S., "Massive Graphical Processing Unit Parallelization for Multirotor Computational Fluid Dynamics," *Journal of Aircraft*, 2023, pp. 1–7. doi:https://doi.org/10.2514/1.C037356.

[29] Cornelius, J. K., Schmitz, S., and Kinzel, M. P., "Efficient Computational Fluid Dynamics Approach for Coaxial Rotor Simulations in Hover," *Journal of Aircraft*, Vol. 58, No. 1, 2021, pp. 197–202. doi:https://doi.org/10.2514/1.C036037.

[30] Sukra Helitek, "RotCFD: Rotor Computational Fluid Dynamics Integrated Design Environment," Version 0.9.15 Build 402, 2020. URL http://sukra-helitek.com/.

[31] Rajagopalan, R. G., Baskaran, V., Hollingsworth, A., Lestari, A., Garrick, D., Solis, E., and Hagerty, B., "RotCFD — A Tool for Aerodynamic Interference of Rotors: Validation and Capabilities," *Future Vertical Lift Aircraft Design Conference*, San Francisco, California, 2012.

[32] Rajagopalan, R. G., Thistle, J. R., and Polzin, W. J., "The Potential of GPU Computing for Design in RotCFD," *AHS Specialists' Conference on Aeromechanics Design for Transformative Vertical Flight*, San Francisco, California, 2018.

[33] Mathur, S. R., and Murthy, J. Y., "A Pressure-Based Method for Unstructured Meshes," *Numerical Heat Transfer, Part B: Fundamentals*, Vol. 31, No. 2, 1997, pp. 195–215. doi:https://doi.org/10.1080/10407799708915105.

[34] NASA, "NASA OVERFLOW Overset Grid CFD Flow Solver," Version 2.4b, 2022. URL https://overflow.larc.nasa.gov/.

[35] Spalart, P. R., and Allmaras, S. R., "A one-equation turbulence model for aerodynamic flows," *30th Aerospace Sciences Meeting and Exhibit*, Reno, Nevada, 1992. doi:https://doi.org/10.2514/6.1992-439, AIAA 1992-439.

[36] Koning, W. J. F., "Wind Tunnel Interference Effects on Tilt Rotor Testing Using Computational Fluid Dynamics," Tech. Rep. NASA/CR-2016-219086, NASA Ames Research Center, Moffett Field, California, March 2016.